





Electric field-induced giant columns of polarized water molecules

Cheng Dai ¹, Maijia Liao ¹, Xiaolin Li,¹ Shuyu Chen,¹ Ping Gao ², and Ping Sheng ^{1,*}

¹*Department of Physics, Hong Kong University of Science and Technology, Clear Water Bay, Kowloon, Hong Kong, China*

²*Department of Chemical and Biological Engineering,*

Hong Kong University of Science and Technology, Clear Water Bay, Kowloon, Hong Kong, China



(Received 15 March 2022; accepted 2 August 2022; published 29 August 2022)

In confined nanoscale structures, such as nanopores or nanotubes, the polar characteristic of water can be evident; while in bulk or droplet form, it is masked by the statistical molecular arrangements dictated by free energy minimization. In this paper, we show that, under an applied electric field, the polar character of water molecules enables the formation of macroscopic scale columns of water vapor penetrating through a silicone oil bath. These columns are up to 60 μm in length and tens of microns in cross-sectional dimension. We have directly visualized such columns by using water-soluble fluorescent molecules dispersed in silicone oil. The polar nature of columns is evidenced by the measured giant electrorheological effect that correlates with the application of an electric field. We present a phenomenological theory to support our observations and show that the experimental data are consistent with a state of highly aligned water molecular dipoles within each column.

DOI: [10.1103/PhysRevResearch.4.033164](https://doi.org/10.1103/PhysRevResearch.4.033164)

I. INTRODUCTION

Water molecules are polar [1,2], each with an electric dipole moment of 1.85 Debye. Hydrogen bonding in this case represents the strong short-range component of the polar interaction between the water molecules. Unlike water in bulk or droplet form, the polar characteristic of water molecules confined in nanopores or nanotubes can be made evident [3–7]. Under an electric field, the lowest energy state of the macroscopic (induced) dipoles is known to be an aligned chain structure. This is evidenced in the case of electrorheological (ER) fluid [8], where the dispersed solid particles in an insulating liquid, each carrying an induced dipole under an applied electric field, were observed to form ordered chains [9,10]. By spanning the two electrodes, the polarized chains offer resistance to shear and thereby alter the rheological property of the composite fluid—from a Newtonian fluid [11] in zero field to a Bingham fluid [12] with a finite yield stress under an applied electric field.

In contrast to the classical ER fluids, for nanosized molecules, the electric-field-induced chain structures of induced dipoles are very unlikely unless the electric field is extremely large. This is obvious from the free energy expression $F = U - TS$, where F is free energy, U denotes internal energy, T means (room) temperature, and S is entropy in units of the Boltzmann constant k_B . As $U \sim \alpha E^2$, where α denotes molecular polarizability, whereas $TS \sim k_B T$, the latter can be much larger than the former, unless the electric field exceeds

10^6 V/cm, which is way beyond the usual macroscopic breakdown field. This disparity in the magnitude between entropy and internal energy is because the polarizability α for an induced dipole is (upper-)bounded by the size of the molecules. Hence, the dominance of the entropy effect would prevent the formation of aligned molecular chains.

The giant ER (GER) effect [13–17] represents another type of ER effect in which the bonding force between the solid particles can be much stronger than that for a conventional ER fluid with induced dipoles. It was found through molecular dynamics (MD) simulations that, in the case of the GER effect, the strong bonding between the solid particles is mediated by molecular dipolar filaments [15,18]. Molecular dipoles can have strong short-range polar interactions, as exemplified by the hydrogen bonding. However, in such cases, the maximization of hydrogen bonds per polar molecule becomes dominant, favoring clusters of various shapes, as in the case of water molecular clusters [19–21]. Application of an electric field, unless it is extremely large, cannot break up such clusters. Hence, the macroscopic phase of aligned molecular dipoles has remained experimentally elusive.

By using the software package GROMACS, it was found that, for a system of urea-enveloped nanoparticles dispersed in silicone oil, the urea molecules can form short, bundled, and polarized filaments that penetrate the silicone oil chains to link the neighboring solid nanoparticles along the electric field direction. It should be noted that, for molecular dipoles, entropy considerations are much more unfavorable to the formation of aligned chains than polarized macroscopic particles, where the temperature essentially plays no role. Here, the silicone oil apparently played an important role as a confining medium that limits the orientational degree of freedom for the molecular dipoles. The GROMACS simulations quantitatively explained the GER effect that can give rise to a yield stress as high as 130 kPa. However, simulations also showed that there exists a maximum length of the bundled urea filaments, ~ 9

*sheng@ust.hk

Published by the American Physical Society under the terms of the [Creative Commons Attribution 4.0 International license](https://creativecommons.org/licenses/by/4.0/). Further distribution of this work must maintain attribution to the author(s) and the published article's title, journal citation, and DOI.

nm, above which the filaments cannot be formed. Due to the small length scale of the urea filaments, direct observation is difficult if not impossible.

We present a simple phenomenological theory, detailed below, that shows, in contrast to urea molecules, for water molecules, there may exist no upper limit to the length of the dipolar filaments, apart from the entropy considerations that can prevent the length to diverge. For a water molecule, its nonlinear shape and the strong hydrogen bonding between the molecules can also imply a columnar structure, instead of single molecular filaments, to best preserve the average number of hydrogen bonds per molecule as close as possible to that of bulk water. In earlier works, it was shown through MD or Monte Carlo simulations that, in a confined one-dimensional (1D) nano-environment, such as inside a carbon nanotube, water molecules can form a dipole-aligned filament [3,4,6,7,22,23]. Here, we show experimentally that, under an applied electric field, macroscopic-scale dipolar columns can penetrate through the silicone oil; they not only can be visualized but also exhibit the GER effect with a well-defined static yield stress. Predictions of the phenomenological theory are in excellent agreement with the experimental data. The experimental results, supported by the agreement with theory, point to a macroscopic, coherent phase of water molecular dipoles induced by an electric field.

This paper is organized as follows. In Sec. II, we introduce a phenomenological theory to explain the structure of the water molecular dipoles induced by an applied electric field. In Sec. III, we present the fabrication method and the measurement platform. In Sec. IV, we report the direct confocal visualization of such giant water columns, up to 60 μm in length and $> 10 \mu\text{m}$ in lateral size, as well as the measured GER effect with a well-defined static yield stress. We conclude with a brief recapitulation in Sec. V.

II. A PHENOMENOLOGICAL THEORY

A. Orientation energy and its dependence on spatial dimension

Consider a single polar molecule in an applied field, in the absence of dipole-dipole interactions. The dipole-field interaction energy is given by $-\vec{p}_0 \cdot \vec{E} = -p_0 E \cos\theta$, where $p_0 = 1.85$ Debye, and θ is the angle between the direction of the dipole moment and the electric field. In a thermal bath, the thermally averaged dipole moment is given by

$$\begin{aligned} \langle p \rangle_{3D} &= \frac{\int_0^\pi p_0 \cos\theta \exp\left(\frac{p_0 E \cos\theta}{k_B T}\right) 2\pi \sin\theta d\theta}{\int_0^\pi \exp\left(\frac{p_0 E \cos\theta}{k_B T}\right) 2\pi \sin\theta d\theta} \\ &= p_0 \left[\coth\left(\frac{p_0 E}{k_B T}\right) - \frac{k_B T}{p_0 E} \right], \end{aligned} \quad (1)$$

for a random dispersion of molecular dipoles in three-dimensional (3D) space. However, if the dipolar orientations are defined by a surrounding medium so that the orientational angle is limited to be either 0 or π , then we have the 1D case:

$$\langle p \rangle_{1D} = \frac{p_0 \exp\left(\frac{p_0 E}{k_B T}\right) - p_0 \exp\left(-\frac{p_0 E}{k_B T}\right)}{\exp\left(\frac{p_0 E}{k_B T}\right) + \exp\left(-\frac{p_0 E}{k_B T}\right)} = p_0 \tanh\left(\frac{p_0 E}{k_B T}\right). \quad (2)$$

At room temperature and the relevant electric field of 5 kV/mm, the value of $p_0 E/k_B T \cong 8 \times 10^{-3} \ll 1$; hence, $\langle p \rangle_{1D} \cong [(p_0)^2/k_B T]E$. The polarizability of the molecular dipole of water $[(p_0)^2/k_B T] \sim 83 \text{ \AA}^3$ is > 50 times larger than the known induced polarizability of the water molecule [24] $\sim 1.5 \text{ \AA}^3$, both in units of $4\pi\epsilon_0$. This large disparity shows that the effect of the permanent molecular dipole dominates over any induced polarization effect for water molecules. It also shows that even a relatively weak electric field can have a much larger effect in aligning molecular dipoles than in a system of nonpolar molecules.

The difference in the thermally averaged dipole moment between the 3D case and the 1D case is given by

$$\begin{aligned} \Delta p &= \langle p \rangle_{1D} - \langle p \rangle_{3D} \\ &= p_0 \left[\tanh\left(\frac{p_0 E}{k_B T}\right) - \coth\left(\frac{p_0 E}{k_B T}\right) + \frac{k_B T}{p_0 E} \right], \end{aligned} \quad (3)$$

which is always positive for any electric field E . The negative energy difference $-\Delta p \cdot E$ thus favors the formation and penetration of 1D water molecular filaments into the porous silicone oil. The magnitude of this energy difference is given by

$$\begin{aligned} \Delta E_{in} &= \Delta p \cdot E \\ &= k_B T \left\{ \frac{p_0 E}{k_B T} \left[\tanh\left(\frac{p_0 E}{k_B T}\right) - \coth\left(\frac{p_0 E}{k_B T}\right) \right] + 1 \right\}. \end{aligned} \quad (4)$$

Here, ΔE_{in} increases with increasing electric field and saturates when the electric field tends to infinity, so that

$$\lim_{E \rightarrow \infty} \Delta E_{in} = k_B T. \quad (5)$$

Equation (5) tells us that water molecules prefer to form 1D filaments in their penetration into porous silicone oil. Compared with the thermally oriented 3D case, this energy difference increases with E until saturation at $k_B T$.

B. Thermally averaged number of molecules in a filament

Water is immiscible with silicone oil, which means that each water molecule has a positive (repulsive) interaction energy σ [25–27] with silicone oil, where σ represents an energetic barrier for a water molecule to penetrate the porous silicone oil. In anticipation of the subsequent development, let us initially assume that water molecules would form a 1D filament inside the silicone oil environment. Then the thermally averaged number of water molecules in such a filament may be expressed by

$$\langle N_{fi} \rangle_\sigma = \sum_{N_{fi}=0}^{\infty} N_{fi} \left[\frac{\exp\left(-\frac{\sigma N_{fi}}{k_B T}\right)}{\sum_{N_{fi}=0}^{\infty} \exp\left(-\frac{\sigma N_{fi}}{k_B T}\right)} \right] = \frac{1}{\exp\left(\frac{\sigma}{k_B T}\right) - 1}, \quad (6)$$

so that the average length of the filament is given by $\langle N_{fi} \rangle_\sigma l$, where $l = 2.8 \text{ \AA}$ is the size of the water molecule [28,29]. When the gap between two surfaces is larger than $2\langle N_{fi} \rangle_\sigma l$, no filament can span across the gap.

In the presence of dipolar interactions, the true energy barrier for the formation of a 1D filament should be $\sigma' = \sigma - \Delta p \cdot E - \Delta_{int}$ for $E > E_c$, where E_c represents a critical electric field for the formation of the filaments, and Δ_{int} denotes the intermolecular dipole-dipole interaction, i.e., the

hydrogen bonding energy. The existence of an E_c , empirically observed in our experiments to be approximately $E_c \cong 0$ to 0.5 kV/mm, is hypothesized to arise from the following plausible scenario. In the absence of an applied electric field, there is already a small number of water molecules in the silicone oil in accordance with the solubility of water in silicone oil. At E_c , the randomly oriented, individually dispersed dipoles become sufficiently aligned so that, through the long-range dipolar interactions, they would self-assemble into filamentary segments by overcoming the entropy barrier. Since the effective dipole of each segment can be much larger than that of the individual molecule, this self-assembly process can cascade into longer segments until the filaments coalesce into columns that span the two electrodes.

It follows from the above that the revised average number of polar molecules in a single-molecule filament is given by

$$\langle N_{\text{fi}} \rangle_{\sigma'} = \frac{1}{\exp\left(\frac{\sigma'}{k_B T}\right) - 1} = \frac{1}{\exp\left(\frac{\sigma - \Delta p \cdot E - \Delta_{\text{int}}}{k_B T}\right) - 1}. \quad (7)$$

Once $\sigma' = 0$, then $\langle N_{\text{fi}} \rangle_{\sigma'}$ would diverge. Moreover, if $\sigma' < 0$, then there is no barrier for the water molecules to enter the silicone oil at $E > E_c$, if they are part of the long filaments.

Since the charges of the water molecule are distributed on 3 sites, in addition to the energetic consideration of the strong hydrogen bonding, it is much more likely for water molecules to form columns rather than single molecular filaments. In that case, the energy barrier σ should be renormalized to $\sigma_r \ll \sigma$ on the per molecule basis since the repulsive interaction with the silicone oil can only be experienced by the surface molecules of the columns; that would favor the formation of long columns even more.

For the water molecule, the volume is $\sim 0.03 \text{ nm}^3$, or $\sim \frac{1}{3}$ of that for the urea molecule [30], the molecular weight of water is also $\sim \frac{1}{3}$ of urea. That can imply a much smaller repulsive energy barrier σ than the urea molecule. If that is the case and the condition $\sigma' < 0$ is satisfied, then $\langle N_{\text{fi}} \rangle_{\sigma'}$ can be very large, i.e., water filaments much longer than 9 nm, even on the order of microns or more, should be attainable. Our experimental observations in Sec. IV confirm this to be the case.

C. Electrical energy density

The energy density of a collection of giant dipoles at a given electric field should include both the dipole-field interaction energy and the dipole-dipole repulsive interaction. To calculate the energy density quantitatively, we introduce an effective surface charge density λ , directly related to the surface number density of the exposed net charges at the electrode-oil interfaces, so that the energy density under an electric field of E can be written as a function of λ as

$$f(\lambda) = \frac{1}{2\epsilon_r \epsilon_0} \lambda^2 - \lambda E. \quad (8)$$

Here, $\epsilon_r = 2.6$ is the relative dielectric constant of silicone oil [31]. In Eq. (8), we have reduced the dipole-dipole and dipole-field interaction energies in the bulk to the interaction energies of the exposed net charges at the end points of the dipolar columns. This is because the column formation has neutralized the net charges in the bulk. The first

term of Eq. (8), the repulsive energy term, is derived from the method of virtual work for a charge layer at a distance d from the metallic boundary, here treated as the perfect conductor (PEC). The result is independent of d . Details of the derivation and its numerical verification are presented in Sec. IV A. Equation (8) is minimized when $\lambda = \epsilon_r \epsilon_0 E$, with the minimum free energy density given by

$$f(\lambda)_{\text{min}} = -\frac{1}{2} \epsilon_r \epsilon_0 E^2 = -11.51 E^2. \quad (9)$$

This equilibrium electrical energy density represents the net electrical energy input into the system by the external electric field. It is shown below in Sec. IV D that $f(\lambda)_{\text{min}}$ directly correlates with the measured pressure drop ΔP , as the manifestation of the GER static yield stress.

D. Area density of filaments

If we regard the column to comprise multiple aggregated water filaments, then for a single filament $60 \mu\text{m}$ in length, there are $N_{\text{fi}} = 60 \mu\text{m}/l \approx 2 \times 10^5$ water molecules. Due to the confining effect created by the surrounding silicone oil molecules plus the dipole-dipole interaction, it has been demonstrated through Monte Carlo simulations that, for a 1D filament with $< 10^6$ molecules, almost all the molecular dipoles must be oriented in a unique direction [6]. Hence, the thermally averaged dipole moment of each water molecule within a filament is given by $\langle p \rangle_{\text{fi}} = p_0$. Apparently, the aligned dipole-dipole interaction energy within the column/aggregated filaments, plus the dipole-field interaction energy, not only can overcome the energy barrier σ , but the excess over σ may also be a few times of $k_B T$ so that the filament is at its energetic ground state. For the urea molecules, on the other hand, the situation could be different, i.e., $\sigma' > 0$ always, so that only a short molecular segment is possible.

The surface charge density at the electrode surface should be

$$\lambda = \vec{P} \cdot \hat{n} = \gamma \frac{p_0}{l} = \epsilon_r \epsilon_0 E, \quad (10)$$

where γ denotes the (area) number density of molecular filaments in the columns at the electrode-oil interfaces. Here, $E > E_c$, and l is the length of the water molecule. From Eq. (10), the density of filaments per unit area is therefore given by

$$\gamma = \frac{\epsilon_r \epsilon_0 l}{p_0} E, \quad (11)$$

which shows that the area density of the filaments should be proportional to the applied electric field E , which can be supported by the qualitative conclusion from the measured linear variation of the fluorescent intensity with applied electric field, shown below in Sec. IV B.

E. Solubility of water in silicone oil

With the expression for the area number density of water filaments, we can derive the expression for the volume density of water molecules n :

$$n = \frac{\gamma}{l} = \frac{\epsilon_r \epsilon_0}{p_0} E, \quad (12)$$

so that the solubility of water in oil S_w , defined as the weight-to-weight ratio, can be expressed as

$$S_w = \frac{nM_w}{N_A\rho_w} \quad (13)$$

Here, M_w and ρ_w are the molar mass and mass density of water, respectively, and N_A denotes Avogadro's constant. Typically, the saturation solubility of water [32], in the absence of an electric field, is ~ 200 ppm at 25°C . The solubility of water in silicone oil under the electric field will be discussed in detail in Sec. IV E.

F. Yield stress

Associated with the aggregated filaments/column formation of water molecular dipoles is the GER effect. The yield stress τ_Y , defined as the shear stress in the limit of zero shear rate, should be a nonzero constant that varies with the applied electric field. This is a clear sign that the composite fluid is a Bingham fluid. Since the dipole-field interaction energy density in the static limit is given by

$$|-\vec{P} \cdot \vec{E}|_{\text{static}} = np_0E = \epsilon_r\epsilon_0E^2 = 2\Delta P_{\text{static}} = 2\tau_Y. \quad (14)$$

Hence, $2\tau_Y/n$ should be linearly proportional to the applied electric field, which is a signature of the GER effect. The yield stress of the aggregated filaments/column is verified experimentally in Sec. IV F to satisfy Eq. (14).

III. SETUP AND MEASUREMENTS

A. Setup

In Fig. 1(a), we show a schematic picture of the experimental setup designed both to observe the polarized water molecular columns as well as to measure their attendant GER effect under an applied electric field. The setup is made of a silicon wafer on top and an indium tin oxide (ITO)-coated glass slide at the bottom to confine the silicone oil (Sigma, 10 cst) that can flow in the channel thus created. The top and bottom walls of the channel are separated by a $60\text{-}\mu\text{m}$ -thick polymethyl methacrylate (PMMA) slice with a $4\text{ mm} \times 2\text{ cm}$ rectangular hole in the center. In the central region of the silicon wafer, a square region with dimensions of $4 \times 4\text{ mm}^2$, denoted the active region, was etched with $28\text{-}\mu\text{m}$ -diameter holes arranged in a triangular array with a lattice constant of $35\text{ }\mu\text{m}$, which will be described in the next subsection. The electric field was applied across the $60\text{ }\mu\text{m}$ gap in this active region. Water vapor enters through the hole array from above, provided via a thermally insulated duct from a remote water reservoir maintained at 80°C (see Fig. 2). A gold film, 150 nm thick, was sputtered on the bottom of the porous silicon region to serve as the top electrode counter to the bottom ITO electrode, which has a thickness of $1.2\text{ }\mu\text{m}$. A porous ultrahigh molecular weight polyethylene (UHMWPE) membrane [33,34], 100 nm in thickness with an average pore size of 50 to 100 nm , was fixed to the electrode. It served the purpose of repelling the silicone oil while allowing the water vapor to easily pass through. Two inlets (labeled 1 and 2) and two outlets (labeled 3 and 4) for the silicone oil were installed on the silicon wafer, as shown in Fig. 1(a). Inlet 2 and outlet 3 were connected to a pressure sensor that can

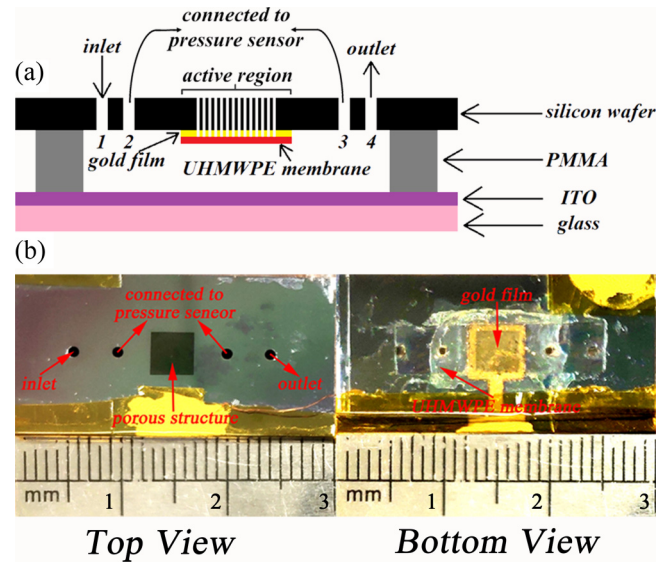


FIG. 1. (a) Schematic picture of the experimental setup. Here, 1 and 4 denote the inlet and outlet for the silicone oil, and 2 and 3 are connected to the pressure sensor. From top to bottom, the structure comprises an etched silicon wafer, a gold film coated on the etched part of the silicon wafer, the porous membrane, the polymethyl methacrylate (PMMA) separator, and indium tin oxide (ITO)-coated glass slide. (b) Photo images of the top and bottom views of the actual sample.

measure the pressure difference between the two ends when the silicone oil was driven at a constant but very low flow rate by a syringe pump. Since both the glass slide and the ITO electrode are transparent, the setup allowed direct confocal microscopy observation of the sample in the active region when an electric field was applied.

B. Fabrication

To permit water vapor to enter the setup shown in Fig. 1(a), a porous structure arranged in a triangular array was fabricated by the Deep Reactive-Ion Etching (DRIE) [35] in the Nano Fabrication Facility at HKUST. Scanning electron microscopy images of the top and cross-sectional views of the porous

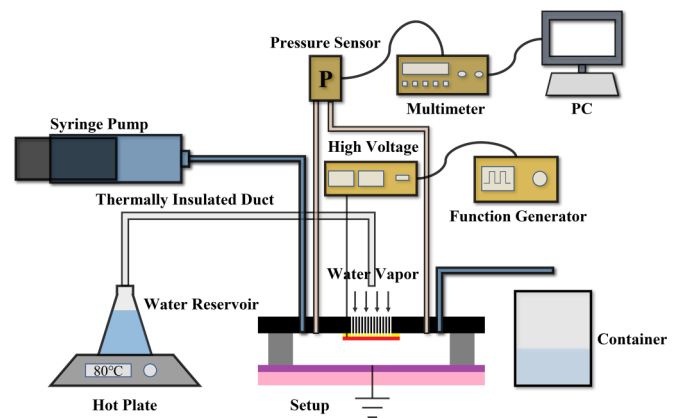


FIG. 2. Schematic illustration of the platform used to measure the pressure drop that resulted from the giant electrorheological (GER) effect of the polar water molecular filaments.

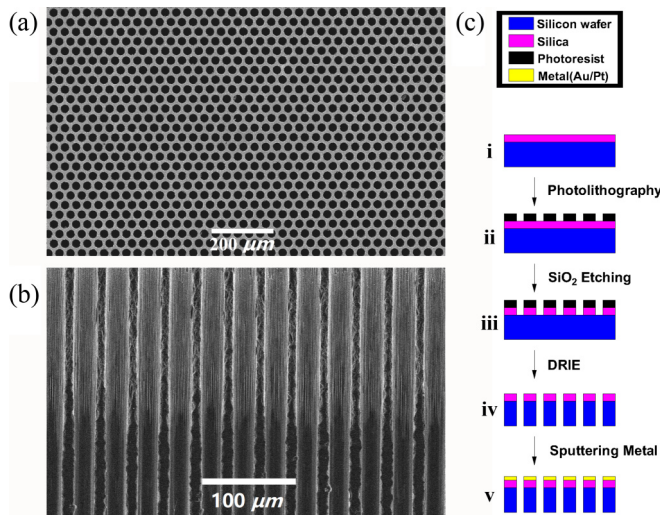


FIG. 3. (a) and (b) Scanning electron microscopy images of the top and cross-sectional views of the etched porous silicon structure in the active region of the sample. The holes are arranged in a triangular array with a lattice constant of $35 \mu\text{m}$, with a hole diameter of $28 \mu\text{m}$. (c) Process flow of etching the porous structure and sputtering the metal as the electrode.

structure are illustrated in Figs. 3(a) and 3(b). The triangular hole array has a lattice constant of $35 \mu\text{m}$, with the hole diameter of $28 \mu\text{m}$. The porosity of the structure is $\sim 60\%$, which permits a high permeation rate of water vapor.

The process flow for fabricating the etching pattern on a silicon wafer is illustrated in Fig. 3(c). A silicon wafer with $3 \mu\text{m}$ oxide was chosen as the starting point. A photoresist was spin-coated on the wafer before defining the photolithography pattern by a photomask. The wafer was hard baked in the oven at 120°C for half an hour after developing the photoresist. The silica layer was overetched to transfer the pattern from the photoresist, which functioned as the mask during the DRIE process. A 150 nm gold layer was sputtered on the surface after the DRIE process to function as the upper electrode.

In fabricating the flow setup, a porous UHMWPE membrane was fixed to the electrode; it was used to allow the water vapor to easily pass through, while excluding the silicone oil. The channel was carved from a PMMA slice and double spin-coated with an optical adhesive (Norland, NOA 61). The cross-section of the flow channel is $\sim 4 \times 0.06 \text{ mm}^2$. PMMA was used since it has a high elastic modulus to prevent any noticeable strain in response to the electrostatic attractive force between the electrodes under an applied electric field. A transparent ITO bottom electrode was used to allow the visualization of the water columns with inverted confocal microscopy (Leica TCS SP5). The square resistance of the ITO layer was $< 1 \Omega$, and the transmittance was $> 70\%$. The silicon wafer, PMMA, and glass were assembled and irradiated by ultraviolet light (Dymax, 5000-EC) for 10 min to fully cure the optical adhesive. The sample was then placed in the oven at 50°C for 12 h to enhance the bonding.

C. Visualization and measurement

To visualize the water filaments under different electric fields in a z -stack form, inverted confocal microscopy was used to capture the images. Here, z -stack just means the collection of all the confocal frames with different z values. The setup was filled with silicone oil, dispersed with the highly water-soluble fluorescent probe 8-hydroxypyrene-1,3,6-trisulfonic acid trisodium salt (HPTS; Thermo Fisher Scientific) at 10 mM concentration. Water vapor molecules were added through the porous structure from a remote water reservoir maintained at 80°C , passing through a heat-insulated duct. HPTS has a maximum absorption at $454 \pm 3 \text{ nm}$ and maximum emission at $512 \pm 4 \text{ nm}$. A 458 nm laser line was used to excite the HPTS, and the emission band ranged from 468 to 568 nm .

The experimental data in Figs. 4 and 5 were measured with the platform shown in Fig. 2. Pure silicone oil with viscosity of 10 cst was used as the working fluid. A syringe pump (Harvard Apparatus, PHD2000) was used to drive the silicone oil through the channel from the inlet to the outlet at a fixed, slow flow rate. A high-voltage source (Spellman, SL10*30),

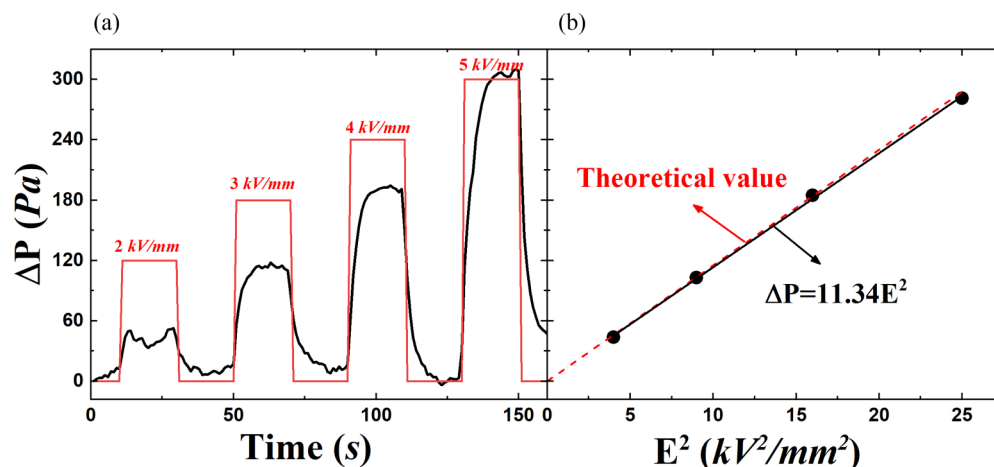


FIG. 4. (a) Pressure drop ΔP relative to the case of zero electric field, measured at a low flow rate of 5 mL/h under the application of square-wave voltage pulses that increased with time. (b) ΔP variation plotted as a function of E^2 . Here, the black line is the linear fitting to the data, shown as the solid black circles. The red dashed line denotes the theory prediction of Eq. (9).

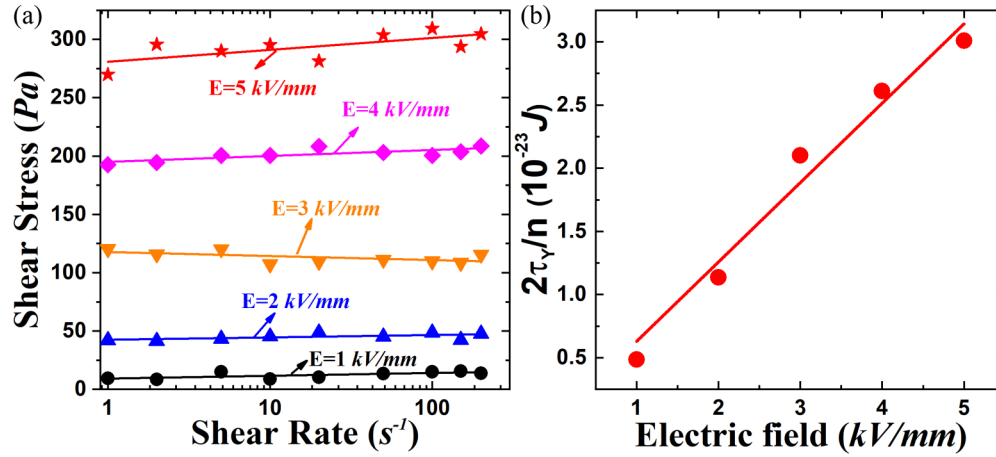


FIG. 5. (a) Shear stress is plotted as a function of shear rate, under different electric field in steps of 1 kV/mm. A nonzero yield stress can be obtained from the zero shear rate intercept of the straight-line fitting to the data, which is the yield stress. Since the flow rate has always been low, the slopes are nearly flat. (b) The yield stress divided by the number density of water molecules $2\tau_y/n$ is shown to display a linear variation with the electric field. The solid circles denote the experimental data; the solid line denotes the best linear fitting. The slope of the fitting line is 1.88 ± 0.07 Debye, very close to the value of the dipole moment of the water molecule, 1.85 Debye.

controlled by the function generator (Tektronix, AFG31022), supplied high voltage. A differential pressure sensor with 1 psi range (Honeywell, 142PC01D) was utilized to convert the pressure drop into electrical signals, measured by the Multimeter (Agilent, 34401A) and recorded by the Labview program.

IV. RESULTS AND DISCUSSIONS

A. Repulsive part of the free energy density

The expression for the repulsive part of the energy density in Eq. (8) can be derived by using the method of virtual work [36,37]. By approximating the charge layer as a continuum surface charge density λ , situated at a distance d from the metallic electrode, here treated as a PEC, the energy of the system can be easily obtained analytically. We used numerical simulations to verify the expression for the case when the charge layer comprises discrete charges arranged in a triangular lattice.

The starting point of the analytical derivation is the observation that, for a continuous two-dimensional layer of charge density, the expression for $\lambda(xd)$ is given by

$$\lambda(xd) = \frac{q}{\frac{\sqrt{3}}{2}(xd)^2}, \quad (15)$$

where x denotes the ratio of the triangular lattice constant to d , and q is the exposed net charge of one water dipole, defined by p_0/l . The total electrostatic energy in a volume V of the Wigner-Seitz cell, with thickness d between the charge plane and the PEC boundary, can be expressed as a function of λ :

$$W(\lambda) = \frac{1}{2}q\phi = \frac{1}{2}q\left(\frac{\lambda}{\epsilon_r\epsilon_0}d\right), \quad (16)$$

where ϕ is the electric potential difference between the surface charge plane and the PEC boundary. The repulsive energy density $f_{re}(\lambda)$ can be evaluated by the principle of virtual work

as

$$\begin{aligned} f_{re}(\lambda) &= \frac{dW}{dV} = \frac{1}{\sqrt{3}xd^2} \frac{dW}{d\lambda} \frac{d\lambda}{d(xd)} = -\frac{1}{2\epsilon_r\epsilon_0} \left[\frac{q}{\frac{\sqrt{3}}{2}(xd)^2} \right]^2 \\ &= -\frac{\lambda^2}{2\epsilon_r\epsilon_0}, \end{aligned} \quad (17)$$

which is just the repulsive part of the energy density given in Eq. (8). The minus sign here denotes that, as the lattice constant increases, the energy density decreases, i.e., the interaction is repulsive. It is noted that Eq. (17) is independent of d .

If the charges are treated as discrete point charges, the repulsive energy density can be numerically evaluated by the virtual work method by using the COMSOL finite element solver to numerically obtain the solution of the Poisson equation for a periodic triangular array of discrete point charges placed near the PEC boundary. For the discrete charge array, there can be electric field lines extending beyond a distance d from the PEC boundary, i.e., the fringing field lines. To capture the electrostatic energy of the fringing field lines [38], the Wigner-Seitz cell is extended to have a total thickness of $6d$ from the PEC boundary. Periodic boundary conditions are applied in the lateral plane. The repulsive energy density is numerically evaluated as the difference in the electrostatic energy divided by the difference of volume in the zone between the charge plane and PEC boundary, with lattice constants of $[xd + \Delta(xd)]$ and xd . Here, $\Delta(xd)$ is taken to be $0.01(xd)$. In Fig. 6, the repulsive energy density is plotted as a function of the square of average charge density under different values of d . The solid symbols denote the simulated values, while the dashed line denotes the analytical solution for the continuum charge density case. The simulated values are seen to match well with the analytical solution, independent of d .

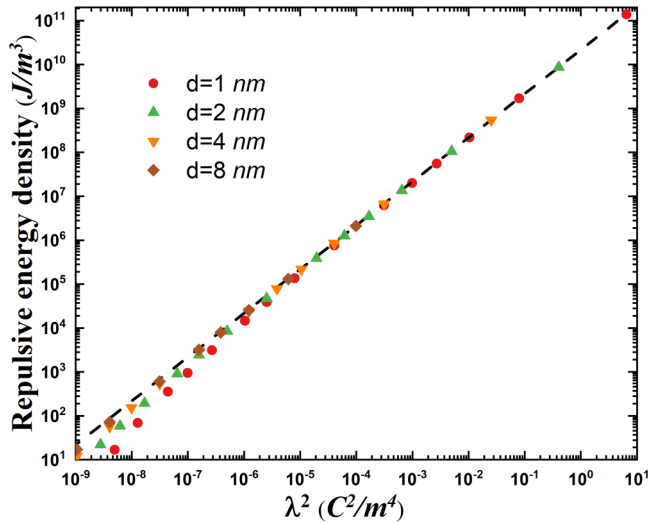


FIG. 6. Repulsive energy density plotted as a function of λ^2 under different separations between the charge plane and perfect conductor (PEC) boundary. Here, symbols denote simulated values with discrete charges, and the dashed line represents the analytic solution with the continuous charge density. The deviation of the simulated results can be attributed to the incomplete capture of the fringing fields when the discrete charges are far apart.

B. Experimental observation of the linearity of area density of filaments with increasing electric field

Fluorescent probe HPTS was used to visualize the water columns by using the confocal microscopy. Water columns were formed by applying an electric field larger than a critical value E_c . In Eq. (11), the area density of the filaments is shown to be proportional to the applied electric field E , and this linear relation can be directly verified experimentally. In Figs. 7(a)–7(d), we show the cross-sectional images captured by the confocal microscope at a plane in the middle of the channel (the plane denoted by the white dashed line in Fig. 8),

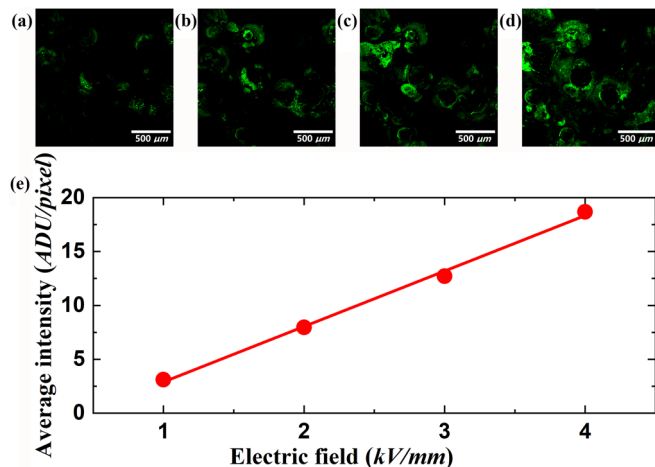


FIG. 7. (a)–(d) Fluorescent images of cross-sections of water filaments under 1–4 kV/mm of applied electric field in 1 kV/mm steps. (e) Average fluorescence intensity (ADU/pixel) variation plotted as a function of the applied electric field. Dots denote the experimental data. The line denotes the linear fitting.

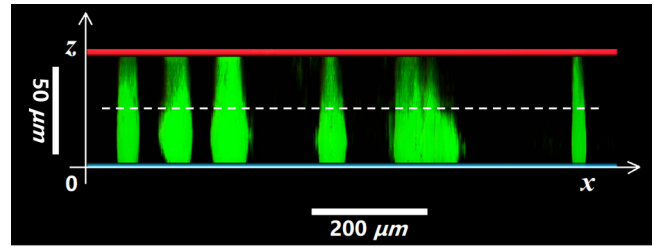


FIG. 8. A sideways view of the three-dimensional (3D) image captured by confocal microscopy, with the fluorescent probe being excited at 458 nm. The emission band ranges from 468 to 568 nm. The scale in the z direction is (stretched to) 3 times that along the x direction. The top and bottom electrodes, separated by $60 \mu\text{m}$ (slightly larger than the vertical scale bar), are shown as the red and blue lines, respectively. The white dashed line indicates the plane at which the cross-sectional images shown in Fig. 7 were taken.

under 1 kV/mm to 4 kV/mm of applied electric field in 1 kV/mm steps. Each frame consists of 1024×1024 pixels. The fluorescent intensity, denoted by pixel value, is indicative of the number density of the aggregated water filaments in each column. In Fig. 7(e), we plot the average fluorescent intensity in analog-to-digital units (ADU) per pixel, defined as the ratio of the summation of all the bright pixels above a fixed brightness threshold to the number of pixels in each frame. A good linear relationship between the average fluorescent intensity and electric field is seen, which implies that the area density of water filaments in the columns increased linearly with the applied electric field. This linear relationship is important in lending support to the measured GER effect, shown below.

C. Confocal observation of water molecular columns

By applying an electric field of 2 kV/mm across the channel, followed by the introduction of water vapor, images in the z -stack were captured and processed to exhibit the 3D sideways view, as shown in Fig. 8. It is seen that the dispersed fluorescent molecules in water brightly illuminate a multiple columnar structure with the maximum length of $60 \mu\text{m}$; some of the columns are seen to span the whole channel height, while others seem to have shorter lengths. It should be noted, however, that, from Fig. 7, the large columns are not solid inside but can comprise many thinner columns/aggregated filaments, as evidenced on the upper side of the thick columns. In Fig. 8, the visual effect is affected by the inhomogeneous spatial distribution of the fluorescent molecules, which tend to aggregate and gradually sediment to the bottom ITO side of the cell. That can account for the brighter illumination on the bottom side. The diameter of these columns is on the order of tens of microns. This image of the fluorescent probe presents direct evidence to show that the water molecules were aligned to form aggregated filaments of varying cross-sectional dimensions, bundled together to form the thick columns. All the columns are rather straight; they may be regarded as 1D in nature. During the column formation process, some bubbles were produced near the surface of electrodes, mainly due to the presence of the conductive component that can enhance the electrolysis of water. We also like to note that the formation of columns is a common manifestation of the well-known

ER effect in which the polarized chains tend to aggregate into columns with the body-centered tetragonal (BCT) structure [18,39,40] of the polarized entities inside the columns. In contrast, due to the hydrogen bonding between neighboring water molecules, the structure inside the columns can differ from simple BCT symmetry, to be further investigated.

D. Manifestation of the GER effect

The fact that the visualized columns are polar in character can be evidenced by the measured GER effect that correlates with the application of an electric field. In the GER effect experiment, pure silicone oil with a viscosity of 10 cst was used to minimize the effect from the electrolysis of water.

In Fig. 4(a), the red line denotes the applied square-wave pulsed electric field whose magnitude increased with time. A constant but slow flow rate of 5 mL/h was imposed by a syringe pump. The measured pressure drop ΔP , relative to that when no electric was applied, is shown by the black line. It is seen that ΔP tends to increase with increasing voltage until a breakdown occurs, at which a maximum $\Delta P = 300$ Pa is attained at 5 kV/mm. Since the active region of our setup has a square geometry, we can infer from Darcy's law [41] that the effective viscosity of the fluid, which in this case must be proportional to ΔP , should have increased due to the formation of water molecular columns perpendicular to the flow direction. We have also performed a reference experiment in which the water vapor was shut off from the measuring system. In that case, $\Delta P = 0$ regardless of the applied electric field value. As ΔP represents the extra energy density input to the system by an applied electric field, it must be equal in magnitude to the equilibrium electrical energy density, as predicted by the right-hand side of Eq. (9), $11.51E^2$. In Fig. 4(b), we can see a clear linear variation of ΔP as a function E^2 , with a dimensionless slope of 11.34. This is in excellent agreement with the theory prediction of Eq. (9), with a slope of 11.51. The latter is only 1.5% higher.

E. Solubility of water molecules in silicone oil

From the measured linear variation of the fluorescent intensity as a function of the applied electric field, we have demonstrated that the area number density of the illuminated pixels is proportional to E . This relation agrees well with the theory expression, Eq. (11). We can also derive the area number density from the measured pressure drop shown in Fig. 4(b). By combining Eqs. (9) and (11), we get $\gamma = 2(\Delta P)/p_0E$. Hence, the values of γ can be obtained from the measured pressure drop shown in Fig. 4(b). They are plotted in Fig. 9(a) as solid circles, with the dashed line denoting the theoretical value from Eq. (11). Good consistency can be seen. Based on the above expression of γ , we can also obtain the solubility $S_w = 2(\Delta P)M_w/p_0EN_A\rho_w$ in terms of the measured pressure drop. The experimental and theoretical values of water solubility in silicone oil are plotted in Fig. 9(b), with solid circles being the experimental data and the line being the theory prediction from Eq. (13). Again, good consistency is seen.

Typically, the saturation solubility of water [32], in the absence of an electric field, is ~ 200 ppm at 25 °C, which is

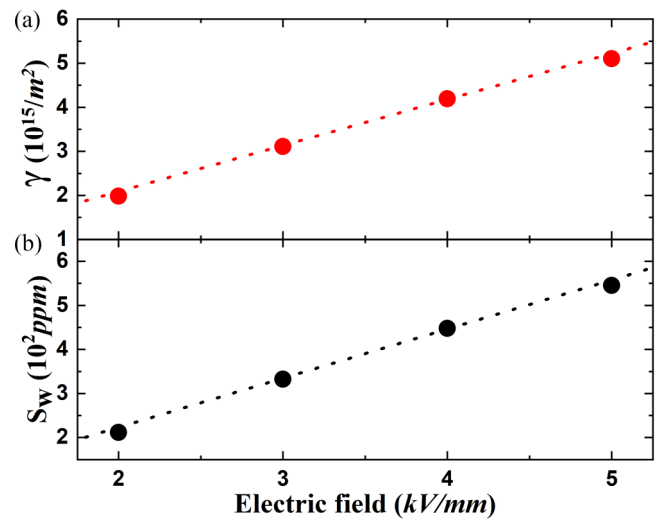


FIG. 9. (a) Area number density of water filaments on the electrode-oil interfaces. (b) Solubility of water molecules in the silicone oil. Dots are values derived from experimental values, while lines denote theoretical values from Eq. (11) and (13). Here, $M_w = 18$ g/mol and $\rho_w = 1 \times 10^3$ kg/m³ are molar mass and density of water, respectively.

much smaller than 550 ppm under 5 kV/mm electric field. Hence, we can draw the conclusion that, by applying an electric field, the water saturation limit in silicone oil can be greatly increased, owing to the favorable formation energy of water dipolar columns above E_c .

An important point to be noted here is that, if the dipoles in the columns were not highly aligned, i.e., taking the value of $\langle p \rangle_{ID}$ instead of p_0 in Eq. (11), then since $\langle p \rangle_{ID} \propto E$ under the relevant conditions, the value of γ would be field independent. This is in contradiction to the experimental data, as shown in Fig. 7. Furthermore, replacing p_0 by $\langle p \rangle_{ID}$ in Eq. (12) will give an unphysically large water solubility in silicone oil that is orders of magnitude higher than the known value.

F. Yield stress

To verify the validity of Eq. (14), shear stress varying with shear rate under different electric fields is plotted in Fig. 5(a). By fitting the shear stress with a linear function, the intercept with the zero-shear-rate axis gives the yield stress. From Eq. (14), $2\tau_y/n$ should be linearly proportional to the applied electric field. Moreover, the slope should be the dipole moment of the water molecule. In Fig. 5(b), an approximate linearity can indeed be observed, and the slope of the fitting line is 1.88 ± 0.07 Debye, very close to the dipole moment of the water molecule. In view of the good agreement between theory and experiment shown in Fig. 4(b), this result should not be a surprise. However, it does show that there must be a high degree of orientational polarization of the dipoles within each column, without which the consistency between the theory and experimental results cannot be achieved.

The maximum yield stress might seem small as compared with the previously measured GER yield stress in other systems. This discrepancy is because, in the latter, there can be very large local field in the region of close approach, on the

order of nanometers or less, between two solid nanoparticles with high dielectric constants. Such a local field is two to three orders of magnitude larger than what is achievable in the present system without incurring an electrical breakdown.

V. CONCLUSIONS

To recapitulate, we have visualized a coherent phase of water molecules induced by an applied electric field, with the GER effect as a manifestation of such a molecular state. A phenomenological theory yields predictions in excellent agreement with the experiment. We deduce the solubility of water molecules (in the form of water vapor) in silicone oil and show that it can be significantly increased through the

application of an electric field. Since water molecules are almost everywhere, with strong electric field not uncommon at the microscopic scale (e.g., in those systems that carry surface charges), we speculate that such a dipole-aligned coherent phase of water may even be present in the natural environment.

ACKNOWLEDGMENTS

P.S. would like to acknowledge the support of Hong Kong Research Grants Council Grant No. 604211 for the initial stage of this research during 2011–2014. P.S. and C.D. would also like to thank W. Wen for allowing us to use his laboratory and the equipment therein. P.S. would like to thank K. Zhang of Göttingen University for his support of this experiment.

-
- [1] S. Meng, L. F. Greenlee, Y. R. Shen, and E. Wang, Basic science of water: challenges and current status towards a molecular picture, *Nano Res.* **8**, 3085 (2015).
- [2] E. Brini, C. J. Fennell, M. Fernandez-Serra, B. HribarLee, M. Luksic, and K. A. Dill, How water's properties are encoded in its molecular structure and energies, *Chem. Rev.* **117**, 12385 (2017).
- [3] R. Pomès and B. Roux, Free energy profiles for H conduction along hydrogen-bonded chains of water molecules, *Biophys. J.* **75**, 33 (1998).
- [4] D. J. Mann and M. D. Halls, Water Alignment and Proton Conduction Inside Carbon Nanotubes, *Phys. Rev. Lett.* **90**, 195503 (2003).
- [5] S. Vaitheeswaran, J. C. Rasaiah, and G. Hummer, Electric field and temperature effects on water in the narrow nonpolar pores of carbon nanotubes, *J. Chem. Phys.* **121**, 7955 (2004).
- [6] J. Köfinger, G. Hummer, and C. Dellago, Macroscopically ordered water in nanopores, *Proc. Natl. Acad. Sci. USA* **105**, 13218 (2008).
- [7] Y. Tu, P. Xiu, R. Wan, J. Hu, R. Zhou, and H. Fang, Water-Mediated signal multiplication with y-shaped carbon nanotubes, *Proc. Natl. Acad. Sci. USA* **106**, 18120 (2009).
- [8] A. van Blaaderen, M. Dijkstra, R. van Roij, A. Imhof, M. Kamp, B. W. Kwaadgras, T. Vissers, and B. Liu, Manipulating the self assembly of colloids in electric fields, *Eur. Phys. J.: Spec. Top.* **222**, 2895 (2013).
- [9] W. Wen, H. Ma, W. Yim Tam, and P. Sheng, Anisotropic dielectric properties of structured electrorheological fluids, *Appl. Phys. Lett.* **73**, 3070 (1998).
- [10] H. Ma, W. Wen, W. Y. Tam, and P. Sheng, Dielectric electrorheological fluids: theory and experiment, *Adv. Phys.* **52**, 343 (2003).
- [11] J. P. Abulencia and L. Theodore, *Fluid Flow for the Practicing Chemical Engineer* (John Wiley & Sons, Hoboken, 2011), Vol. 11.
- [12] R. P. Chhabra, Non-Newtonian fluids: an introduction, in *Rheology of Complex Fluids*, edited by J. Krishnan, A. Deshpande, and P. Kumar (Springer, New York, 2010), pp. 3–34.
- [13] W. Wen, X. Huang, S. Yang, K. Lu, and P. Sheng, The giant electrorheological effect in suspensions of nanoparticles, *Nat. Mater.* **2**, 727 (2003).
- [14] H. Jie, M. Shen, J. Xu, W. X. Chen, Y. Jin, W. N. Peng, X. B. Fu, and L. W. Zhou, Enhancement of local electric field in an electrorheological system, *Appl. Phys. Lett.* **85**, 2646 (2004).
- [15] S. Chen, X. Huang, N. F. A. van der Vegt, W. Wen, and P. Sheng, Giant Electrorheological Effect: A Microscopic Mechanism, *Phys. Rev. Lett.* **105**, 046001 (2010).
- [16] X. Liu, J. Guo, Y. Cheng, G. Xu, Y. Li, and P. Cui, Synthesis and electrorheological properties of polar molecule-dominated TiO₂ particles with high yield stress, *Rheol. Acta* **49**, 837 (2010).
- [17] K. Lu and R. Shen, The characteristics of polar molecule ER fluids and a new type of polar molecule ER fluid, *Smart Mater. Struct.* **26**, 054005 (2017).
- [18] P. Sheng and W. Wen, Electrorheological fluids: mechanisms, dynamics, and microfluidics applications, *Annu. Rev. Fluid Mech.* **44**, 143 (2012).
- [19] K. Liu, J. D. Cruzan, and R. J. Saykally, Water clusters, *Science* **271**, 929 (1996).
- [20] S. Maheshwary, N. Patel, N. Sathyamurthy, A. D. Kulkarni, and S. R. Gadre, Structure and stability of water clusters (H₂O)_n, n = 8–20: an *ab initio* investigation, *J. Phys. Chem. A* **105**, 10525 (2001).
- [21] J. D. Smith, C. D. Cappa, K. R. Wilson, B. M. Messer, R. C. Cohen, and R. J. Saykally, Energetics of hydrogen bond network rearrangements in liquid water, *Science* **306**, 851 (2004).
- [22] G. Hummer, J. C. Rasaiah, and J. P. Noworyta, Water conduction through the hydrophobic channel of a carbon nanotube, *Nature (London)* **414**, 188 (2001).
- [23] B. Mukherjee, P. K. Maiti, C. Dasgupta, and A. K. Sood, Jump reorientation of water molecules confined in narrow carbon nanotubes, *J. Phys. Chem. B* **113**, 10322 (2009).
- [24] J. N. Israelachvili, *Intermolecular and Surface Forces* (Academic Press, London, 2011).
- [25] L. Zhu, Y. Jin, Q. Xue, X. Li, H. Zheng, T. Wu, and C. Ling, Theoretical study of a tunable and strain-controlled nanoporous graphenylene membrane for multifunctional gas separation, *J. Mater. Chem. A* **4**, 15015 (2016).
- [26] Z. Yuan, A. Govind Rajan, R. P. Misra, L. W. Drahushuk, K. V. Agrawal, M. S. Strano, and D. Blankshtein, Mechanism and prediction of gas permeation through sub-nanometer graphene pores: comparison of theory and simulation, *ACS Nano* **11**, 7974 (2017).

- [27] X. Liang, S. Ng, N. Ding, and C. L. Wu, Enhanced hydrogen purification in nanoporous phosphorene membrane with applied electric field, *J. Phys. Chem. C* **122**, 3497 (2018).
- [28] J. S. D'Arrigo, Screening of membrane surface charges by divalent cations: an atomic representation, *Am. J. Physiol. Cell Physiol.* **235**, C109 (1978).
- [29] M. Gerstein and C. Chothia, Packing at the protein-water interface, *Proc. Natl. Acad. Sci. USA* **93**, 10167 (1996).
- [30] W. Stein, *Transport and Diffusion Across Cell Membranes* (Elsevier, Amsterdam, 2012).
- [31] R. M. Hakim, R. G. Olivier, and H. St-Onge, The dielectric properties of silicone fluids, *IEEE Trans. Electr. Insul.* **EI-12**, 360 (1977).
- [32] P. Przybylek, Water saturation limit of insulating liquids and hygroscopicity of cellulose in aspect of moisture determination in oil-paper insulation, *IEEE Trans. Dielectr. Electr. Insul.* **23**, 1886 (2016).
- [33] P. Gao, J. Li, R. Li, Q. Zhang, and Q. Gu, *Method for Synthesis of Flexible Multifunctional High-voidage Ultrathin PE Membranes* (2020), U.S. Patent App. 16/642,316.
- [34] A. K. Oktavius, Q. Gu, N. Wihardjo, O. Winata, S. W. Sunanto, J. Li, and P. Gao, Fully-conformable porous polyethylene nanofilm sweat sensor for sports fatigue, *IEEE Sensors J.* **21**, 8861 (2021).
- [35] Y. Q. Fu, A. Colli, A. Fasoli, J. K. Luo, A. J. Flewitt, A. C. Ferrari, and W. I. Milne, Deep reactive ion etching as a tool for nanostructure fabrication, *J. Vac. Sci. Technol. B* **27**, 1520 (2009).
- [36] J. Coulomb and G. Meunier, Finite element implementation of virtual work principle for magnetic or electric force and torque computation, *IEEE Trans. Magn.* **20**, 1894 (1984).
- [37] A. J. Deeks and J. P. Wolf, A virtual work derivation of the scaled boundary finite-element method for elastostatics, *Comput. Mech.* **28**, 489 (2002).
- [38] V. Leus and D. Elata, *Fringing Field Effect in Electrostatic Actuators*, Technion-Israel Institute of Technology Technical Report No. ETR-2004-2 (2004).
- [39] R. Tao and J. M. Sun, Three-Dimensional Structure of Induced Electrorheological Solid, *Phys. Rev. Lett.* **67**, 398 (1991).
- [40] M. Parthasarathy and D. J. Klingenberg, Electrorheology: mechanisms and models, *Mater. Sci. Eng. R Rep.* **17**, 57 (1996).
- [41] S. P. Neuman, Theoretical derivation of Darcy's law, *Acta Mech.* **25**, 153 (1977).